Available online at www.sciencedirect.com
SCIENCE DIRECT
Acta Materialia 54 (2006) 1501–1511
Acta MATERIALIA
www.actamat-journals.com

Load partitioning in aluminum syntactic foams containing ceramic microspheres

Dorian K. Balch [1], David C. Dunand *

Department of Materials Science and Engineering, Northwestern University, Evanston, IL 60208, USA

Received 9 February 2005; received in revised form 15 November 2005; accepted 16 November 2005
Available online 24 January 2006

Abstract

Syntactic foams were fabricated by pressure-infiltrating liquid aluminum (commercial purity and 7075-Al) into a packed preform of silica–mullite hollow microspheres. These foams were subjected to a series of uniaxial compression stresses while neutron or synchrotron X-ray diffraction measurements of elastic strains in the matrix and the microspheres were obtained. As for metal matrix composites with monolithic ceramic reinforcement, load transfer in the pure aluminum foams is apparent between the two phases during elastic deformation, and is affected at higher stresses by matrix plasticity. Calculating effective stresses from the lattice strains shows that the microspheres unload the pure aluminum matrix by a factor of about 2. In the aluminum alloy foams, an in situ reaction between silica and the melt leads to the conversion of silica to alumina in the microsphere walls and the precipitation of silicon particles in the matrix. This affects the load transfer between the matrix and the reinforcement (microspheres and particles), and increases the macroscopic foam stiffness by over 40%, as compared to the pure aluminum foams. Composite micromechanical modeling provides good predictions of the elastic moduli of the syntactic foams, capturing the effects of load transfer and suggesting that significant stiffness improvements can be achieved in syntactic foams by the use of microspheres with stiff walls and/or by the incorporation of a stiff reinforcing phase within the metallic matrix.

Keywords: Aluminum; Foams; Synchrotron X-ray diffraction; Neutron diffraction; Elastic behavior

1. Introduction

Syntactic metallic foams are a class of metallic foams where closed porosity is produced by embedding hollow ceramic microspheres within a metallic matrix. Because the ceramic microspheres are typically non-wetting, and because their volume fraction must be maximized to achieve low-density foams, syntactic metallic foams are produced by pressure infiltration of a liquid metal (usually aluminum [1,2] or magnesium [3]) into a packed preform of hollow ceramic microspheres, a processing approach used previously for metal matrix composites with monolithic (non-hollow) ceramic reinforcement [4].

In conventional closed-cell metallic foams produced, for example, by gas entrapment, pore collapse occurs at low applied compressive stresses. By contrast, the pores of syntactic foams are surrounded by stiff, strong ceramic shells which delay their deformation and collapse during compressive deformation, and increase the foam stiffness and strength. Thus, these ceramic shells act as reinforcement within the metallic matrix and, as is the case for metal matrix composites [5], load is shared between the metallic matrix and the ceramic comprising the microsphere walls during elastic and plastic deformation of the foam. As long as the shells are not fractured, the hollow microspheres are stronger and stiffer than the voids present in non-syntactic closed-cell foams, and can therefore unload the matrix. To date, this load-sharing mechanism in metallic syntactic

* Corresponding author. Tel.: +1 847 491 5370; fax: +1 847 467 6573.
E-mail addresses: dkbalch@sandia.gov (D.K. Balch), dunand@northwestern.edu (D.C. Dunand).
[1] Present address: Sandia National Laboratories, P.O. Box 969, MS 9035, Livermore, CA 94551, USA.

1359-6454/$30.00
doi:10.1016/j.actamat.2005.11.017

foams has not, to the best of our knowledge, been studied in detail.

Recently, we studied plasticity and damage accumulation in syntactic foams with aluminum matrices and mullite-based hollow microspheres [6]. In the present work, we use these same syntactic foams to investigate the micromechanics of load transfer between the metallic matrix and the ceramic shells. Experimentally, we use synchrotron X-ray and neutron diffraction techniques to determine the elastic lattice strains developing in both phases during uniaxial deformation of the foams, as was done previously for particulate-reinforced metal matrix composites using synchrotron X-rays [7–10] or neutrons [11–16]. We then compare our experimental results to micromechanical elastic calculations, from which predictions concerning stiffness-optimized metallic syntactic foams can be made.

2. Experimental procedures

We studied the same syntactic foams whose fabrication is described in detail in an earlier publication [6], and is thus only summarized briefly here. The ceramic hollow microspheres were provided by Envirospheres PTY Ltd (Lindfield, NSW, Australia) with diameters of 15–75 μm, wall thicknesses of 2–5 μm, and densities of 0.6–0.8 g/cm^3. The microsphere walls consist of a mixture of 45 vol.% crystalline mullite ($3Al_2O_3$–$2SiO_2$) and 55 vol.% amorphous silica. Liquid commercial-purity aluminum (Al) or alloyed aluminum (7075-Al) was pressure-infiltrated at a temperature of about 710 °C into a tapped bed of microspheres and solidified under pressure with a cooling rate of about 10 °C/min. The 7075-Al foam was heat-treated in air for 36 h at 120 °C. Samples for metallography, density measurement, and mechanical testing were machined from the as-infiltrated Al foam or the heat-treated 7075-Al foam. Metallographic samples were polished using SiC paper, followed by 6 and 1 μm water-based diamond suspensions. Foam density was measured by helium pycnometry. The foam shear and Young's moduli were determined ultrasonically, using 2.25 MHz transducers and a digital oscilloscope for both longitudinal and shear wave measurements.

In situ synchrotron X-ray diffraction measurements were performed at the DuPont-Northwestern-Dow Collaborative Access Team (DND-CAT) at Sector 5 of the Advanced Photon Source (Argonne National Laboratory). Using a tabletop load frame, the uniaxial compressive stress on an Al foam sample ($6.63 \times 6.77 \times 14.98$ mm) was varied from 0 to −100 to 0 MPa, in steps of 20 MPa, during which diffraction measurements were obtained at constant applied stress. A 7075-Al foam sample ($4.10 \times 4.13 \times 9.04$ mm) was tested in a similar manner up to stresses of −200 MPa. The samples were subjected to constant uniaxial loads for 900 s (Al) or 1800 s (7075-Al) during irradiation with a monochromatic 65 keV ($\lambda = 0.019$ nm) X-ray beam aligned perpendicular to the sample compression axis. The X-ray beam had a square cross-section of either 0.5×0.5 mm (Al) or 0.75×0.75 mm (7075-Al). The diffracting volumes of 1.66 mm^3 (Al) and 2.31 mm^3 (7075-Al) contained about 25,000–30,000 microspheres. A 132 mm diameter 16-bit charge-coupled device camera (MAR Inc., Evanston, IL) was positioned at a distance of 710 mm from the sample, and captured complete Debye–Scherrer rings. A molybdenum powder reference standard was attached to each specimen for use in the lattice strain calculations. A similar set-up was used in previous studies of metal matrix composites [7,8,10].

In situ neutron diffraction measurements during compression testing were performed at the Lujan Center of the Los Alamos Neutron Science Center (LANSCE) using the Neutron Powder Diffractometer (NPD). Stresses up to −67 MPa (Al foam) and −220 MPa (7075-Al foam) were applied, with measurements made at intervals of 10 MPa (Al) or 20 MPa (7075-Al), and an intermediate series of unloading measurements made at −100 MPa for the 7075-Al foam. The sample sizes were $8.96 \times 8.97 \times 18.74$ mm for the Al sample and $8.98 \times 9.00 \times 18.88$ mm for the 7075-Al specimen. Measurement times ranged from 1 to 2 h for each loading step. The diffracting volumes were considerably larger than those for the X-ray experiments, about 800 mm^3 for both samples. A similar set-up was used in previous studies of load transfer in metal matrix composites [13,15,16]. All diffraction measurements were carried out to maximum applied stresses below the foam peak stress, measured previously as −110 and −230 MPa (with no more than 10% variation) [6].

Analysis of the X-ray diffraction patterns for the mullite and silicon phases was performed as described in detail in Refs. [7,10], and consisted of determining the axial and transverse strains by least-squares fitting of diffraction rings, using custom-written software. This procedure provides volume-averaged strains, without accounting for spatial variations of strains within the microsphere walls. Analysis of neutron diffraction data for the aluminum matrix was performed using the General Structure Analysis System (GSAS) software package [17]. The single peak fitting routine fits the selected diffraction peak with a convolution of Gaussian and exponential peaks (appropriate for spallation neutron spectra) [18], calculating the peak position as the centroid of the fitted peak. Rietveld refinement [19] of complete spectra fits all peaks simultaneously by calculating a theoretical diffraction pattern based on the space groups and lattice constants of the phases present, and then fitting the theoretical spectrum to the experimental data by performing a multi-variable least-squares fit, varying parameters such as the lattice constant, background functions, absorption, extinction, and Debye–Waller factors. [17,20]. As with the X-ray diffraction data, the resulting strains were volume averaged. Neutron measurements of the strains present in the mullite grains proved impossible within reasonable time limits (<5 h/measurement), due to the small volume fraction of crystalline mullite present (~7 vol.%) within each sample and the inherently weak

interactions [21] of neutrons with aluminum, silicon, and oxygen.

3. Results

3.1. Microstructure

Figs. 1(a) and 1(b) show representative scanning electron microscopy (SEM) images for Al and 7075-Al foams. For both types of foams, the microspheres are uniformly distributed, with an apparent average diameter of ~50 μm, and infiltration of the spaces between microspheres is very nearly complete, with no visible porosity remaining between microspheres. Some infiltrated microspheres are seen in both foams (Fig. 1(b) and Ref. [6]): their number fraction, as determined by counting ~6000 microspheres on polished sections, is 4.4% for the Al foams and 9.3% for the 7075-Al foams. Also present in the matrix of both foams (Fig. 1(b) and Ref. [6]) are microsphere fragments formed during either packing or infiltration. The higher number of such fragments in the 7075-Al foam may be due to the dissolution of the microspheres, which occurred preferentially in the alloyed matrix due to its considerably longer solidification time resulting from its large freezing range ($T_{liquidus} = 635$ °C, $T_{solidus} = 477$ °C [22]).

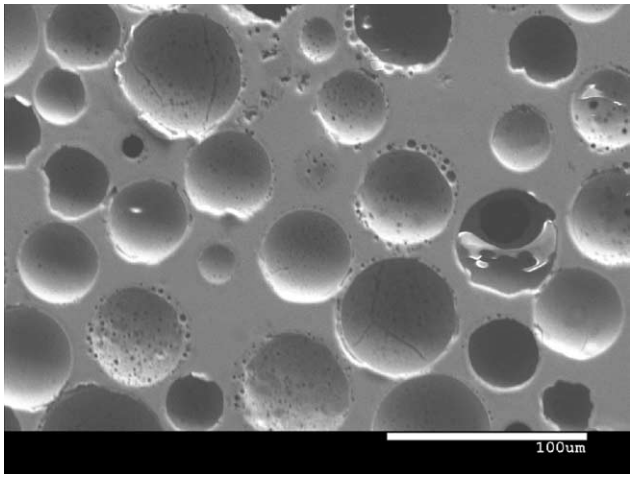

Fig. 1(a). SEM micrograph of polished cross-section of Al foam, showing hollow mullite microspheres within an aluminum matrix.

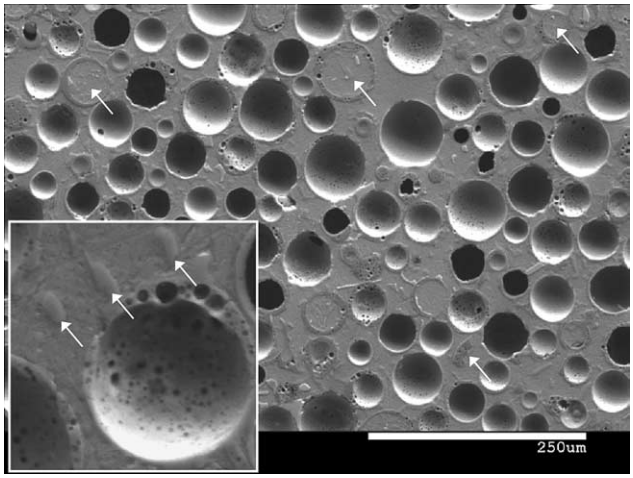

Fig. 1(b). SEM micrograph of polished cross-section of Al–Si foam, showing hollow mullite microspheres within an aluminum matrix containing silicon plates as well as defects (fragmented or infiltrated microspheres, marked by arrows). Inset: SEM micrograph of polished cross-section of Al–Si foam, showing silicon plates (marked by arrows) adjacent to a microsphere.

Also seen in the 7075-Al foams are two types of matrix inclusions: (i) plate-like inclusions, determined to be silicon using energy-dispersive X-ray spectroscopy (EDS) and exhibiting the rounded morphology often seen for silicon in heat-treated aluminum alloys [23]; and (ii) blocky inclusions with a much smaller volume fraction (~1–2%), identified by EDS as an Al–Cr–Fe intermetallic. Image analysis of multiple micrographs for each foam supplied the volume fractions of each phase, shown in Table 1, where "sphere fragments" refer to the shell walls of infiltrated microspheres in addition to fragments of shell material. In both foams, some merged or nested microspheres are observed, but these occur very infrequently and their effect on bulk mechanical properties is neglected. As seen in Fig. 1(b), the silicon plates are often nucleated on the microspheres. Based on average sizes and densities supplied by the manufacturer and SEM observations, the amount of porosity present within the microsphere walls is estimated to be ~35%.

Figs. 2(a) and (b) show EDS maps of a representative microsphere in each of the foams, measured with all settings in the SEM instrument constant. It is apparent that the microspheres in the 7075-Al foams contain more aluminum and less silicon than in those in the Al foam. This is confirmed by EDS point analysis within the microsphere wall, which gives an Al/Si peak ratio of ~1 for the Al foam and ~6 for the 7075-Al foam. Also visible in Fig. 2(b) are the silicon plates in the matrix. Dissolution of silicon from the microsphere walls into the liquid matrix altered the matrix chemistry of the 7075-Al foam, so that the adjusted composition of the matrix is approximately (in wt.%): 23% Si, 4% Zn, 2% Mg, 1% Cu, 0.15% Cr, balance Al [6]. Thus, the 7075-Al foam is hereafter referred to simply as "Al–Si foam", while the commercial-purity foam is called "Al foam". It should be noted that as a result of the changed matrix composition, the heat treatment used (36 h at 120 °C) most likely did not produce a peak-aged matrix.

The average foam densities measured by helium pycnometry are 1.41 and 1.64 ± 0.05 g/cm^3 for the Al and Al–Si foams, respectively, corresponding to relative densities of 0.52 and 0.59 ± 0.02 as compared to the fully

Table 1
Measured volume fractions (%) of foam constituents

Foam matrix	Hollow microspheres	Microsphere fragments	Si	Al matrix
Al	61.8	1.1	0	37.1
Al–Si	57.8	2.3	10.2	29.7[a]

[a] Includes ~1–2% Al–Cr–Fe intermetallic.

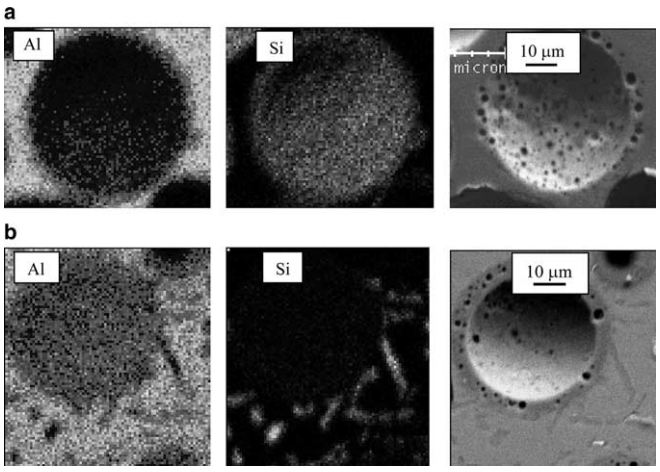

Fig. 2. EDS Maps of representative microspheres in polished sections of (a) Al foam and (b) Al–Si foam. In the Al–Si foam, the microsphere contains more Al and less Si, and the matrix contains Si plates, indicative of the reaction according to Eq. (1).

dense matrix material. Ultrasonic elastic modulus measurements give values for the Young's and shear moduli of $E = 27.8$ and $G = 10.8$ GPa for the Al foam, and $E = 40.0$ and $G = 15.5$ GPa, for the Al–Si foam.

3.2. Diffraction data

Plots of applied compressive stress vs. average lattice strain (measured by either diffraction technique) are shown in Figs. 3 and 4 for Al and Al–Si foams, respectively. Initial residual strains due to thermal expansion mismatch would have the effect of shifting the lattice strain curves along the strain axis, without altering the shapes of the curves, and have been neglected.

For the Al foams, the effect of applied stress on the matrix longitudinal and transverse strain, as measured by neutron diffraction, is shown in Figs. 3(a) and 3(b), respectively. Due to the large aluminum grain size in both foams, X-ray matrix strain data were either unobtainable or of lower quality than the neutron measurements. Despite the larger diffracting volume in the neutron experiments, complete spectra containing all lattice peaks could not be obtained for the Al foam; instead, peaks from one or two matrix grains were obtained at each detector. The most intense of these peaks were used to calculate strains by single-peak fitting: the {3 1 1} peak in the axial direction and

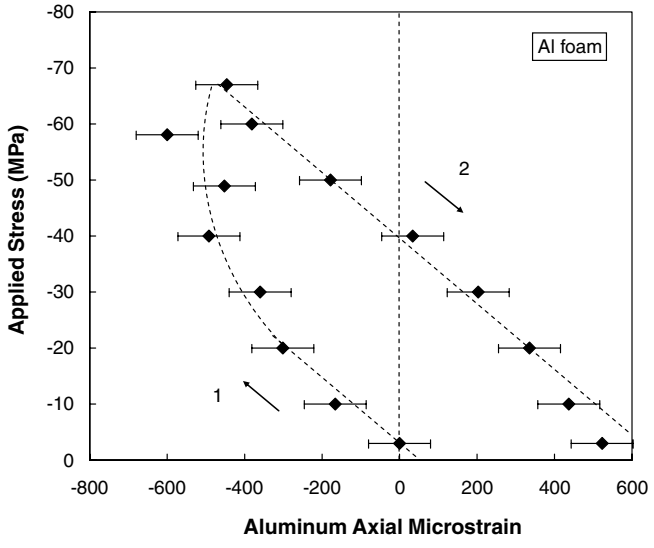

Fig. 3(a). Al foam: aluminum matrix axial lattice strains (neutron, {3 1 1} peak) as a function of applied compressive stress on loading (arrow 1) and subsequent unloading (arrow 2). The unloading dashed line is a best-fit line through the unloading data. A line of the same slope is used for the low-stress loading data, and is connected in a smooth manner through the high-stress loading data (where matrix plasticity takes place) to the unloading line. Error bars are ±80 με.

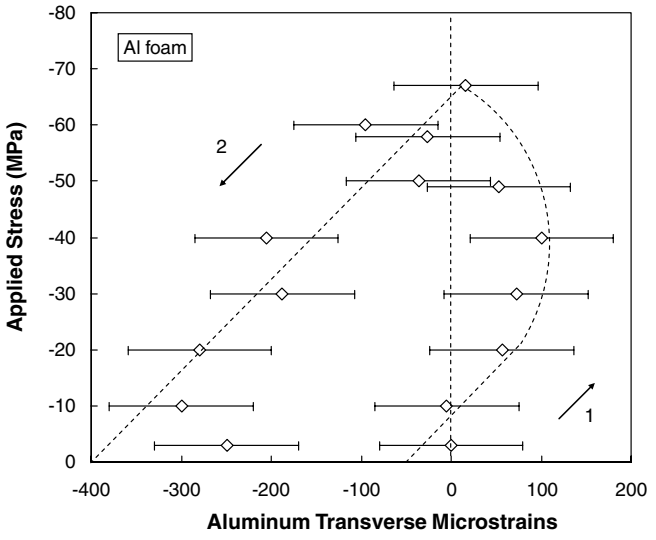

Fig. 3(b). Al foam: aluminum matrix transverse lattice strains (neutron, {2 2 0} peak) as a function of applied compressive stress. Dashed lines and arrows are as per Fig. 2(a). Error bars are ±80 με.

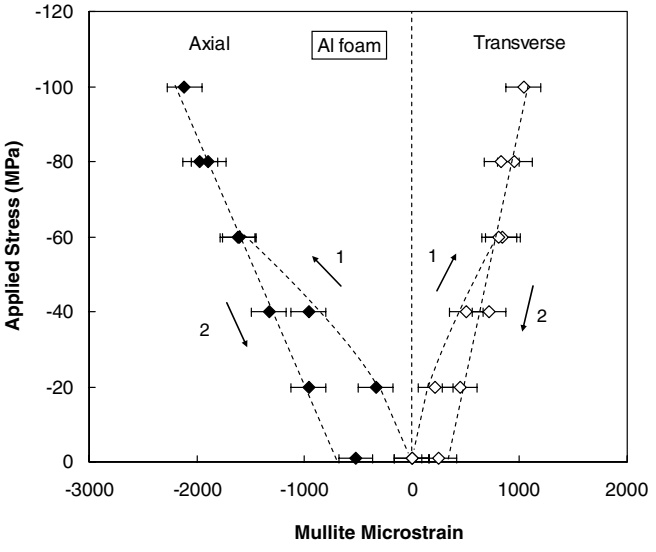

Fig. 3(c). Al foam: mullite axial and transverse lattice strains (X-ray, {1 2 0} + {2 1 0} ring) as a function of applied compressive stress. Dashed lines and arrows are as per Fig. 3(a). Error bars are ±160 με.

the {220} peak in the transverse direction. The Young's moduli perpendicular to these planes are 69.0 and 72.6 GPa, respectively, close to the isotropic polycrystalline average of 70.3 GPa for pure aluminum [24]; the strains measured along these crystallographic directions should therefore be representative of the average strains in the matrix. The axial and transverse strains within the mullite grains in the microsphere walls of the Al foam are shown in Fig. 3(c), as measured by X-ray diffraction using the {120} + {210} rings. These rings (resulting from the fine grain size of mullite) are the most intense, but overlap in the diffraction patterns due to both the similar *d*-spacings of the planes (0.341 and 0.338 nm, respectively) and to geometrical broadening caused by the sample thickness; they were therefore analyzed as a single ring. Using single-crystal elastic constants for mullite [25], the Young's moduli perpendicular to the {120} and {210} planes were calculated as 188 and 220 GPa, respectively, slightly below but fairly close to the polycrystalline average of 228 GPa. Any change in the shape of the overlapping ring due to this difference in stiffness has been neglected.

Figs. 4(a) and 4(b) show for the Al–Si foam the effect of applied stress on the axial and transverse aluminum matrix lattice strains, as measured by neutron diffraction. As the matrix grains were smaller in the Al–Si foam, complete aluminum diffraction spectra were obtained in this material, so the matrix strains could be calculated by Rietveld refinement. The axial and transverse strains within the mullite grains in the microsphere walls for the Al–Si foam, as measured by X-ray diffraction using the {120} + {210} ring, are shown in Fig. 4(c). X-ray strain data were also obtained for the silicon inclusions (for the {111} ring) within the matrix of the Al–Si foam, as shown in Fig. 4(d).

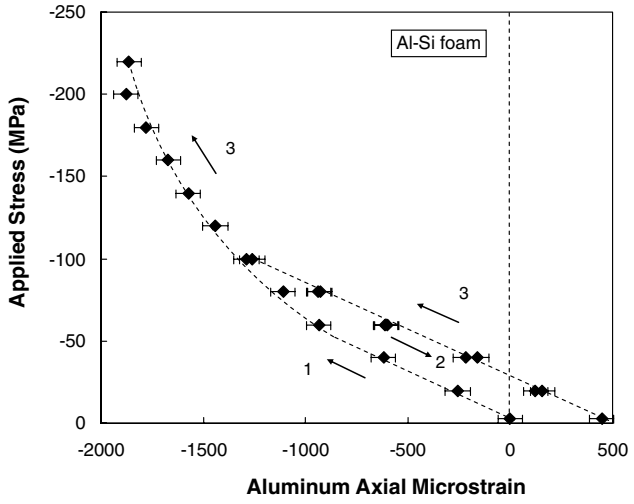

Fig. 4(a). Al–Si foam: aluminum matrix axial lattice strains (neutron, Rietveld), as a function of applied compressive stress on loading (arrow 1), unloading (arrow 2) and reloading (arrow 3). Dashed lines illustrate the change of slope during loading. Error bars are ±60 με.

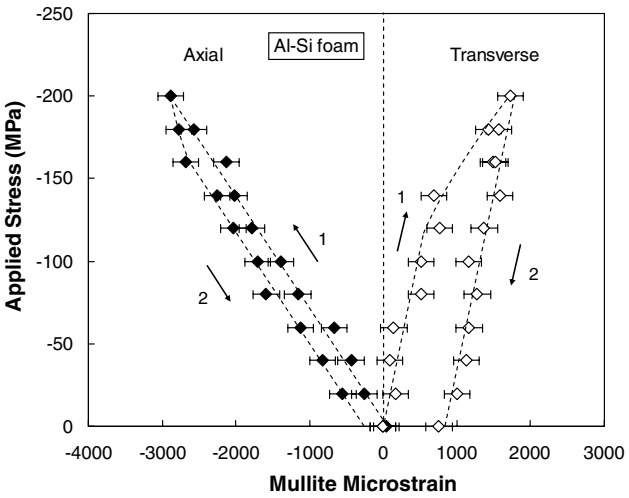

Fig. 4(c). Al–Si foam: mullite axial and transverse lattice strains (X-ray, {120} + {210} rings) as a function of applied compressive stress. Dashed lines and arrows are as per Fig. 3(a). Error bars are ±175 με.

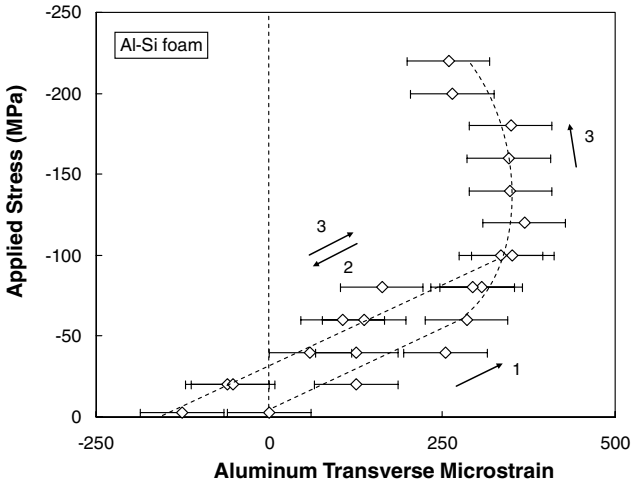

Fig. 4(b). Al–Si foam: aluminum matrix transverse lattice strains (neutron, Rietveld) as a function of applied compressive stress. Dashed lines and arrows are as per Fig. 3(a). Error bars are ±65 με.

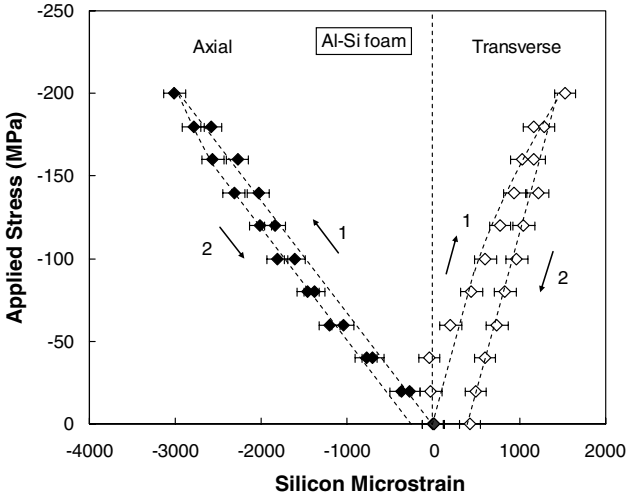

Fig. 4(d). Al–Si foam: silicon axial and transverse lattice strains (X-ray, {111} ring) as a function of applied compressive stress. Dashed lines and arrows are as per Fig. 3(a). Error bars are ±125 με.

4. Discussion

4.1. Displacement reaction in Al–Si foams

The presence of silicon particles in the matrix of Al–Si foams (Fig. 1(b)) and depletion of silicon within the microsphere walls (Fig. 2(b)) indicate that silica present in the spheres walls has reacted with the liquid aluminum according to [26,27]:

$$4Al + 3SiO_2 = 3Si + 2Al_2O_3 \quad (1)$$

The volume fraction of the silicon phase in the Al–Si foams (10.2%, Table 1) is higher than can accounted for if all the silica present in the spheres reacts according to Eq. (1). This can be explained by considering that the foam samples were machined from regions near the centers of the infiltrated billets; such regions were reached during infiltration by liquid metal which had dissolved silicon previously when in contact with the upper regions of the microsphere preform. Such macroscopic segregation has been observed in other composite systems where the melt reacts with the reinforcement [28–30].

We believe that the above reaction occurred in the billet center as well for the following two reasons. First, EDS measurements show a drastic decrease in the amount of silicon present within the sphere walls in the Al–Si foam (Fig. 2(a) and (b)). Second, the measured density for the Al–Si foam (1.64 g/cm^3) is much higher than the predicted value of 1.47 g/cm^3, calculated using the experimentally determined volume fractions of Al matrix, silicon, and unreacted microsphere walls. Based on the stoichiometry of the silica–alumina reaction (Eq. (1)), a given volume fraction of alumina is expected to be produced by a 2:1 mixture (by volume) of silica (from the microsphere wall) and aluminum (from the matrix), respectively. If all silica is reacted, the fraction of alumina in the walls is 25 vol.%, corresponding to an average fraction of alumina in the foam of 5.8 vol.%; this brings the predicted foam density to 1.53 g/cm^3, closer to the measured value (1.64 g/cm^3). Alumina is neither visible as a separate phase in optical or SEM images nor detected in the diffraction experiments. The former may be due to the very fine scale at which alumina is formed within the microsphere walls, while the latter might be explained by the tendency of alumina to form in various lower-symmetry polymorphs during the reaction (Eq. (1)), rather than the typical α-Al_2O_3 corundum, particularly at lower reaction temperatures [27]. It is worth noting that the constituents on the right-hand side of Eq. (1) (after reaction) are stiffer than those on the left-hand side (before reaction), indicating that the in situ reaction will produce a stiffer foam.

4.2. Phase strains in Al foams

On initial compressive loading, the aluminum matrix axial lattice strains (Fig. 3(a)) increase near linearly with the applied stress up to an applied stress $\sigma_a = -30$ MPa, indicating elastic behavior. A direct measure of the effectiveness of elastic load transfer from the matrix to the microsphere reinforcement is the slope of this elastic line, with a higher slope corresponding to lower elastic strain within the phase for a given applied stress, and therefore the presence of lower stresses within the phase. The measured slope in the initial elastic regions of Fig. 3(a) is ~70 GPa for the Al foam. For comparison, the slope for the pure aluminum matrix of a hypothetical foam containing no microspheres (with $\rho^* = 1.41$ g/cm^3, where the shell material is replaced with matrix, i.e., without load transfer) would be $E_s(\rho^*/\rho_s) = 37$ GPa by a stress balance argument. During the initial elastic deformation, the presence of the microsphere is therefore unloading the matrix in the longitudinal direction by a factor of almost two.

At higher stresses, for σ_a between -40 and -67 MPa, the matrix average strain departs from the elastic loading slope significantly, indicating that its rate of loading is much reduced. This behavior is typically observed in metal matrix composites with monolithic reinforcement when the matrix becomes plastic [5], and it is likely that a similar mechanism is active in the present case: the plastically deforming aluminum matrix transfers load to the elastic microspheres. Microsphere cracking is not responsible for the change of slope, as the reduced load-bearing capacity of broken microspheres would increase matrix loading and thus decrease, rather than increase, the slope of the matrix lattice strain curve. Due to the early onset of macroscopic sample plasticity at $\sigma_a = -67$ MPa, this sample was not tested to higher stresses.

Fig. 3(a) shows that, on unloading from the maximum compressive stress, the matrix axial lattice strains increase linearly with a slope close to the original loading line, as expected for an elastic composite. A residual strain of ~0.05% (which is not an absolute value, as mentioned earlier) is accumulated at the end of this mechanical cycle, as also observed in metal matrix composites after plastic deformation of the matrix [5]. The transverse strain evolution (Fig. 3(b)) is similar to the axial behavior: elastic behavior to -30 MPa and plastic deflection to -67 MPa followed by elastic unloading, with a slope similar to the first loading segment. A similar transverse strain behavior is also often seen in metal matrix composites, as a result of the Poisson ratio mismatch between the two phases [5].

As seen in Fig. 3(c), both axial and transverse mullite strains are significant in magnitude, reaching values of -0.21% and 0.10%, respectively, for the highest applied stress $\sigma_a = -100$ MPa. In both the axial and transverse directions, the lattice strains increase roughly linearly up to $\sigma_a = -60$ to -80 MPa. A change of slope due to matrix plasticity is expected, based on stress equilibrium considerations, to occur near $\sigma_a = -30$ MPa as for the matrix in Figs. 3(a) and 3(b). An inflection point is difficult to detect within experimental error in Fig. 3(c), but can be illustrated by the following procedure: (i) a best-fit line is plotted through all unloading data points

between $\sigma_a = -100$ and -3 MPa and (ii) another line with the same slope as the unloading line is plotted through the first loading points. It then appears that the loading line connects, within the large experimental error, the loading points up to a stress $\sigma_a = -20$ to -40 MPa. For higher stresses, both axial and transverse mullite strain curves seem to exhibit a shallower slope, indicative of an increase in load transfer efficiency from matrix to microspheres, in agreement with the previous discussion of matrix plasticity and the decreased load-bearing capacity of the matrix. Given the large experimental error, we cannot exclude the possibility of microsphere collapse occurring at the highest stress, which would become visible as a second inflection point in the loading curves of each phase, with load being transferred back from microspheres to matrix.

In summary, the axial and transverse elastic strains in the Al foam, measured in both matrix and mullite phases in two directions by both neutron and X-ray diffraction in Figs. 3(a), 3(b), 3(c), are consistent with the following series of events occurring during compressive deformation of the foams: (i) elastic loading of matrix and microspheres up to applied stresses of about -30 MPa, with elastic load transfer from matrix to microspheres; (ii) matrix plasticity initiating beyond about -30 MPa, leading to increased load transfer to the microspheres; (iii) elastic unloading of both matrix and microspheres, resulting in residual elastic strains.

4.3. Phase strains in Al–Si foams

The matrix strains in the axial and transverse directions for the Al–Si foam, calculated by averaging over multiple lattice reflections by Rietveld refinement of neutron diffraction measurements, are shown in Figs. 4(a) and 4(b). As expected from this averaging procedure, these strain curves are much smoother than those for the Al foam, which were determined from single diffraction peaks (Figs. 3(a) and 3(b)). The matrix axial behavior for the Al–Si foam (Fig. 4(a)) is qualitatively similar to that of the Al foam. First, an elastic region is visible where load transfer occurs elastically between the matrix and the reinforcement (consisting of microspheres and silicon particles). The matrix slope is ~60 GPa, to be compared to that of a hypothetical pure aluminum foam with $\rho^* = 1.64$ g/cm^3 (corresponding to the Al–Si foam) with a value $E_s(\rho^*/\rho_s) = 43$ GPa. Thus, as for the Al foam, the presence of the reinforcement is unloading the matrix in the longitudinal direction, but by a smaller factor of 1.4. Beyond the elastic range, a sharp departure from the elastic behavior occurs for stresses above -60 MPa, indicative of a reduced rate of matrix loading due to matrix plasticity. After elastic unloading from -100 to -3 MPa and subsequent elastic reloading to -100 MPa, plastic deformation of the matrix continues, as visible from the smoothly increasing strain–stress slope up to $\sigma_a = -220$ MPa (Fig. 4(a)). The transverse matrix strains show more scatter (Fig. 4(b)), as expected from their lower magnitude, but follow the same overall trends as the axial strains.

The X-ray diffraction measurements of mullite and silicon lattice strains are shown in Figs. 4(c) and 4(d) for the Al–Si foam. The mullite axial strains (Fig. 4(c)) follow a near-linear trajectory during loading and unloading, returning to a residual strain near zero. The same illustrative procedure used in Fig. 3(c) indicates the possibility that matrix plasticity (clearly visible in Fig. 4(a)) produces additional load transfer in the microsphere on loading above -60 MPa (Fig. 4(c)). The plastic load-transfer situation is, however, complicated by the presence of the rigid silicon particles dispersed within the aluminum matrix. As illustrated in Fig. 4(d), additional load transfer may be occurring in the silicon particles above -60 MPa when considering the transverse strains.

Based on these diffraction measurements, it appears that the deformation of the Al–Si foam is similar to that of the Al foam, with matrix plasticity initiating at an applied stress of -60 MPa, well below the macroscopic peak stress of the foam (-230 MPa). The onset of microsphere cracking and unloading, which would be visible as upward deviations in the mullite lattice strain curves, was not observed, as the maximum applied stress in the X-ray experiment only reached -200 MPa, sufficiently below the expected peak stress of about -230 MPa.

4.4. Phase stress calculations

The average principal stresses present in each phase can be estimated from the measured average strains using the following equations [31]:

$$\sigma_1 = \frac{E}{1+\nu}\varepsilon_1 + \frac{\nu E}{(1+\nu)(1-2\nu)}(\varepsilon_1+\varepsilon_2+\varepsilon_3), \tag{2a}$$

$$\sigma_2 = \sigma_3 = \frac{E}{1+\nu}\varepsilon_2 + \frac{\nu E}{(1+\nu)(1-2\nu)}(\varepsilon_1+\varepsilon_2+\varepsilon_3), \tag{2b}$$

where σ_1 is the axial principal stress, σ_2 and σ_3 are the transverse principal stresses, ε_1 and ε_2 ($=\varepsilon_3$) are the measured elastic principal strains, E is Young's modulus, and ν is Poisson's ratio of the phase under consideration. For calculations using single-peak strains (all the strains obtained from the Al foam, and the mullite and silicon strains in the Al–Si foam), the plane-specific elastic moduli were used for E, while for calculation of the aluminum stresses in the Al–Si foam (where Rietveld refinement over all diffraction peaks was used to calculate strains), the polycrystalline average modulus was used. The bulk average Poisson's ratio was used for ν in all calculations. For each phase, these principal stresses can in turn be used to determine the average von Mises effective stress, σ_{eff} [31]:

$$\sigma_{eff} = \frac{1}{\sqrt{2}}[(\sigma_1-\sigma_2)^2 + (\sigma_2-\sigma_3)^2 + (\sigma_3-\sigma_1)^2]^{1/2}. \tag{3}$$

The effective stress σ_{eff} in each phase is a measure of the degree to which the applied stress σ_a is partitioned between the different foam constituents. In the absence of load

transfer (i.e., in a single-phase monolithic material) and under uniaxial loading, the effective stress is equal to the magnitude of the applied stress ($\sigma_{eff} = |\sigma_a|$). In composites where stiffness mismatch exists, phases that carry relatively less of the applied stress within the elastic regime display an effective stress lower than the applied stress ($\sigma_{eff} < |\sigma_a|$) and conversely stiffer phases that carry more stress exhibit an effective stress in excess of the applied stress ($\sigma_{eff} > |\sigma_a|$). These effects are intensified if the matrix undergoes plasticity while the reinforcement remains elastic.

The effective stresses calculated from Eqs. (2) and (3) are plotted in Fig. 5 as a function of the applied stress for the aluminum and mullite phases of the Al foam (Fig. 5(a)) and for the aluminum, mullite, and silicon phases of the Al–Si foam (Fig. 5(b)). The unloading and reloading portions of the aluminum matrix data are not shown for clarity. A number of points can be made: (i) in the initial elastic region, the aluminum matrices in both foams bear an effective stress σ_{eff} which is about equal to $|\sigma_a|$, while in the plastic region, σ_{eff} drops to about $|\sigma_a|/2$; (ii) the mullite σ_{eff} values are higher by a factor about four (in the elastic region) to six (in the plastic region) than $|\sigma_a|$ in the Al foam, but only by a factor of two (elastic region) to three (plastic region) in the Al–Si foam; and (iii) the silicon σ_{eff} values are higher by a factor two (elastic region) to three (plastic region) than $|\sigma_a|$ in the Al–Si foam. These observations can be rationalized as follows: (i) despite the significant void space within the foam, the aluminum matrices bear approximately the same stresses as they would in a monolithic aluminum sample in the elastic region, and are therefore considerably unloaded by the microspheres; (ii) the microspheres bear significantly more stress than the matrix and thus act as reinforcement; (iii) load transfer between microsphere and matrix increases as the matrix becomes plastic; and (iv) the reinforcing effect of the microspheres is higher in the Al foam than in the Al–Si foam, because in the latter foam high stresses are carried by the relatively stiff ($E_{Si} = 163$ GPa [24]) silicon particles present within the matrix which act as an in situ formed reinforcement. Also, the replacement of silica with stiffer alumina in the microspheres (Eq. (1)) will lead to a lower average mullite stress.

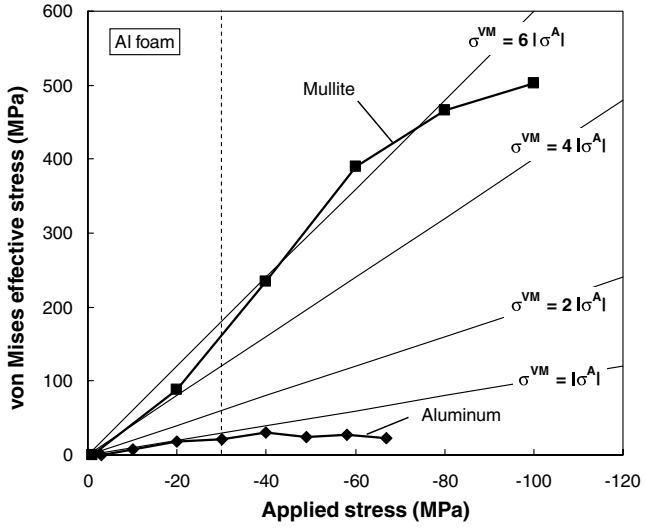

Fig. 5(a). Al foam: plot of von Mises effective stresses (calculated from the measured axial and transverse lattice strains) vs. the applied stress for the aluminum and mullite phases. Solid lines correspond to ratios $\sigma_{eff}/|\sigma_a| = 1$, 2, 4 and 6. Vertical dashed line indicates onset of matrix plasticity and increase of load transfer from matrix to reinforcement.

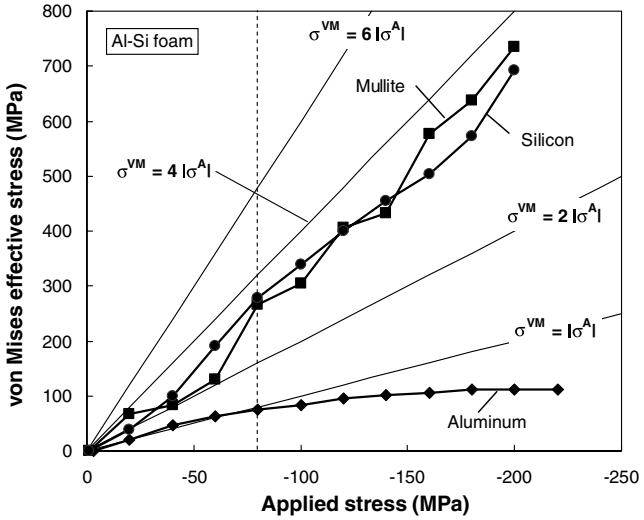

Fig. 5(b). Al–Si foam: plot of von Mises effective stresses (calculated from the measured axial and transverse lattice strains) vs. the applied stress for the aluminum, silicon, and mullite phases. Solid and dashed lines are as per Fig. 5(a).

4.5. Foam stiffness calculations

The experimental evidence discussed above clearly shows that microspheres and silicon particles act as reinforcements within the metallic matrix during compression of these foams. Attempts to predict the stiffness of these materials with scaling laws developed for foams, e.g. Gibson–Ashby predictions of the type $E_{foam} \approx E_{solid}(\rho_{foam}/\rho_{solid})^2$ [32], lead to significant underestimation of Young's modulus by approximately 25–35%, since this model does not take into account the reinforcing effect of the microspheres. We therefore seek to model the stiffness of the foams using composite theories. Two approaches are used: a four-phase self-consistent solution derived for syntactic foam microstructures [33], and a continuum foam model based on three-dimensional finite-element modeling [34]. As both approaches require as inputs the microsphere wall elastic moduli, these average elastic properties are first calculated using a multi-phase Eshelby formulation [35–37]. For the Al foams, we consider a silica matrix containing 30 vol.% mullite inclusions and 35 vol.% voids. These values were calculated using the chemical composition of the microspheres, given by the supplier as 40 wt.% alumina and 60 wt.% silica, and corresponding to 47 vol.% mullite and 53 vol.% silica, based on silica and mullite densities of 2.20 and 3.16 g/cm^3, respectively [38]. Here, the mullite particles and pores are assumed to be spherical, and

sufficiently small relative to the microsphere wall thickness to be treated as inclusions in an Eshelby-type calculation. From Young's and shear moduli values of 73 and 31 GPa for silica, 228 and 89 GPa for mullite [38], and 0 GPa for the pores, the Young's and shear moduli of the wall material were calculated and are listed in Table 2. For the Al–Si foams, we assume that the silica has been replaced by alumina (as discussed previously) and calculate, using the same procedures, elastic constants listed in Table 2. It is apparent that the wall stiffness has more than doubled after silica has been replaced by much stiffer alumina.

4.5.1. Foam stiffness calculations by the four-phase self-consistent method

Bardella and Genna [33] developed explicit solutions for syntactic foam shear and bulk moduli based on a previous extension [39] of the self-consistent method for homogenized modulus estimation [40]. This "four-phase" self-consistent method, which developed elasticity theory modulus solutions considering the central void, microsphere wall material, and matrix material embedded in a surrounding homogenous medium, provides very good agreement with the limited published syntactic polymer foam results in which ceramic microsphere volume fraction is systematically varied [33,41,42]. Using this four-phase self-consistent method, aluminum matrix properties of $E = 70.3$ GPa and $\nu = 0.347$ [24], and microsphere wall properties shown in Table 2, the predicted Young's and shear moduli of the Al foam are 25.9 and 10.1 GPa, within 7% of the measured values and validating our choice of composite-based models to account for the increase in stiffness deduced from the diffraction results. For the Al–Si foam, to avoid implicit systems of equations, we first homogenize the aluminum and silicon in the matrix using the Eshelby method, before incorporating the microspheres in the four-phase model. Using the calculated "matrix" properties of $E = 86.4$ GPa and $\nu = 0.321$ and microsphere wall properties from Table 2, we predict for the Al–Si foam Young's and shear moduli of 42.8 and 16.8 GPa, within ~8% of the measured values.

4.5.2. Foam stiffness calculations by the composite foam method

We use here an empirical equation for the stiffness E^* of a single-phase foam, developed by fitting a large number of three-dimensional finite-element results for large-scale foam models with Voronoi closed cells [34]:

$$\frac{E^*}{E_s} = \left(\frac{(\rho^*/\rho_s) - \rho_0}{1 - \rho_0}\right)^m, \tag{4}$$

where E_s is the Young's modulus of the foam solid material and ρ_s its density. The above equation was found to be valid (and in good agreement with experimental foam measurements) over a range $\rho^*/\rho_s = 0.15$–1.0 with the following parameters: $m = 2.09$ and $p_0 = -0.140$.

We first calculate, using the multi-phase Eshelby formulation [35–37], the Young's moduli of "homogenized" porosity-free composite materials consisting of Al and microsphere wall material (for the Al foam), and Al, Si, and microsphere wall material (for the Al–Si foam); these values are 61.0 and 96.1 GPa, respectively. We then use these values as E_s in Eq. (4) to predict the elastic moduli E^* of the foams. As shown in Table 3, predicted values are in good agreement (±7%) with experimental results. In particular, the large increase in foam stiffness due to the presence of silicon and alumina produced in situ within the matrix and microspheres is correctly predicted.

Similarly, we determine the foam shear modulus G^* using the continuum equation:

$$G^* = \frac{E^*}{2(1+\nu^*)}, \tag{5}$$

where ν^* is the foam Poisson's ratio, which, for relative densities above 0.45, can be approximated by Poisson's ratio of the solid material [34]. The Eshelby method provides values of $\nu^* = 0.293$ and 0.297 for the homogenized composite materials in the Al and Al–Si foams, respectively. Using in Eq. (5) these values and those calculated from Eq. (4) for E^* result in values for G^* which are again in good agreement (±7%) with measurements, as shown in Table 3. The fact that these matrix homogenizations coupled with the empirical relationship in Eq. (4) provide satisfactory predictions of foam stiffness suggest that this relatively straightforward procedure may be adequate for initial design purposes, thereby avoiding the considerably lengthier calculations of the four-phase self-consistent method.

It is instructive to compare the stiffness of the present syntactic Al and Al–Si foams with that of a hypothetical closed-cell pure aluminum foam with the same absolute density ρ^*. We use Eq. (4) with $E_m = 70.3$ GPa (the Young's modulus of aluminum) and $\rho_m = 2.70$ g/cm^3 (the density of aluminum). Eq. (4) predicts that a hypothetical foam containing no microspheres with the same density

Table 2
Calculated elastic constants of microsphere walls

Foam matrix	E_{wall} (GPa)	G_{wall} (GPa)	ν_{wall}
Al	48.8	20.1	0.212
Al–Si	114	46.1	0.234

Table 3
Foam modulus measurements and predictions

Foam matrix	E (GPa)	G (GPa)
Al		
Measurement	27.8	10.8
Four-phase self-consistent prediction	25.9	10.1
Composite foam prediction	26.6	10.3
Al–Si		
Measurement	40.0	15.5
Four-phase self-consistent prediction	42.8	16.8
Composite foam prediction	42.7	16.5

as the present Al foam ($\rho^* = 1.41$ g/cm^3) would exhibit a Young's modulus of 22 GPa, which is ~20% less than the measured value of 28 GPa for the present syntactic Al foam. Similarly, comparing to the present Al–Si foam with $\rho^* = 1.64$ g/cm^3, Eq. (4) predicts a Young's modulus of 28 GPa for a closed-cell aluminum foam without microspheres, a reduction of about 30% as compared to the measured value of 40 GPa. These calculations again illustrate the significant gains in stiffness that can be achieved by the introduction of load-bearing microspheres or silicon plates in the foam.

5. Conclusions

Metal–ceramic syntactic foams were fabricated by liquid metal infiltration, resulting in a percolating network of silica–mullite microspheres embedded within an aluminum matrix (both alloyed and unalloyed). Reaction between melt and silica was found to occur in the alloyed foams, leading to the precipitation of silicon particles in the matrix, and the formation of alumina within the microspheres.

Neutron and synchrotron X-ray diffraction measurements of the elastic strains developed in the foam phases were performed at various static compressive loads, to examine the partitioning of stress within the components of the foams. These measurements indicated that elastic load transfer occurs between the matrix and the microspheres, and is affected by matrix plasticity. By calculating an effective stress from the measured lattice strains, the degree of load partitioning between phases was determined: in the Al foam, it was found that the microspheres unload the matrix by a factor close to 2, while in the stiffer alloyed foam, the in situ formed silicon particles act as reinforcement thus unloading somewhat the microspheres relative to the Al foam.

Two approaches taking into account load transfer between phases of the syntactic foams were used to model the foam Young's moduli: an elastically rigorous four-phase self-consistent formulation, and a second approach in which the microspheres and aluminum matrix were averaged as a composite according to the Eshelby method, and the effect of porosity was then taken into account using a model based on finite-element results. Both methods accurately capture the increase in foam stiffness brought about by load transfer to the reinforcing phases, suggesting that significant improvements in foam stiffness can be achieved by use of microspheres with stiff wall materials, as well as by incorporation in the foam matrix of a stiff reinforcing ceramic phase, either added ex situ or produced in situ, as with the present reaction between liquid aluminum and silica.

Acknowledgments

D.K.B. gratefully acknowledges the US Department of Defense for support in the form of an NDSEG Fellowship. The authors thank Mr. Paul Seshold (Envirospheres PTY Ltd) for providing the microspheres used in the syntactic foams. The neutron diffraction experiments were carried out at the Los Alamos Neutron Science Center, where the help of Drs. Hahn Choo, Don Brown, and Mark Bourke is gratefully acknowledged. The X-ray diffraction experiments were performed at the DuPont-Northwestern-Dow Collaborative Access Team (DND-CAT) at the Advanced Photon Source, where the help of Drs. Denis Keane and John Quintana is greatly appreciated. DND-CAT is supported by the E.I. DuPont de Nemours & Co., the Dow Chemical Company, the US National Science Foundation through Grant DMR-9304725, and the State of Illinois through the Department of Commerce and the Board of Higher Education Grant IBHE HECA NWU 96. Use of the Advanced Photon Source was supported by the US Department of Energy, Basic Energy Sciences, Office of Energy Research under Contract No. W-31-102-Eng-38.

References

[1] Rohatgi PK, Guo RQ, Iksan H, Borchelt EJ, Asthana R. Mater Sci Eng A 1998;244:22.
[2] Kiser M, He MY, Zok FW. Acta Mater 1999;47:2685.
[3] Hall IW, Poteet CJ. Mater Sci Lett 1996;15:1015.
[4] Mortensen A, Jin I. Int Mater Rev 1992;37:101.
[5] Clyne TW, Withers PJ. An introduction to metal matrix composites. Cambridge, UK: Cambridge University Press; 1993.
[6] Balch DK, O'Dwyer JG, Davis GR, Cady CM, Gray GT, Dunand DC. Mater Sci Eng A 2005;391:408.
[7] Wanner A, Dunand DC. Metall Mater Trans A 2000;31:2949.
[8] Wanner A, Dunand DC. J Neutron Res 2001;9:495.
[9] Maire E, Owen A, Buffiere JY, Withers PJ. Acta Mater 2001;49:153.
[10] Balch DK, Ustundag E, Dunand DC. Metall Mater Trans A 2003;34:1787.
[11] Allen AJ, Bourke MAM, Dawes S, Hutchings MT, Withers PJ. Acta Metall Mater 1992;40:2361.
[12] Bourke MAM, Goldstone JA, Shi N, Allison JE, Stout MG, Lawson AC. Scr Mater 1993;29:771.
[13] Dunand DC, Mari D, Bourke MAM, Roberts JA. Metall Mater Trans A 1996;27:2820.
[14] Shi N, Bourke MAM, Roberts JA, Allison JE. Metall Mater Trans A 1997;28:2741.
[15] Daymond MR, Lund C, Bourke MAM, Dunand DC. Metall Mater Trans A 1999;30:2989.
[16] Vaidyanathan R, Bourke MAM, Dunand DC. Acta Mater 1999;47:3353.
[17] Larson AC, Von Dreele RB. GSAS, general structure analysis system. Report No. LAUR 86-748, Los Alamos National Laboratory, Los Alamos (NM); 1994.
[18] Von Dreele RB, Jorgensen JD, Windsor CG. J Appl Cryst 1982;15:581.
[19] Rietveld HM. J Appl Cryst 1969;2:65.
[20] Young RA, editor. The Rietveld method. Oxford, UK: Oxford University Press; 1993.
[21] Bacon GE. Neutron diffraction. 3rd ed. Oxford, UK: Clarendon Press; 1975.
[22] Hatch JE, editor. Aluminum: properties and physical metallurgy. Metals Park (OH): ASM International; 1984.
[23] Metals handbook. 10th ed., vol. 2. Materials Park (OH): ASM International; 1990.

[24] Levy M, Bass HE, Stern RR, editors. Handbook of elastic properties of solids, liquids, and gases, vol. II. San Diego (CA): Academic Press; 2001.
[25] Kriven WM, Palko JW, Sinogeikin S, Bass JD, Sayir A, Brunauer G, et al. J Eur Ceram Soc 1999;19:2529.
[26] Guo RQ, Rohatgi PK. Metall Mater Trans B 1998;29:519.
[27] Yoshikawa N, Kikuchi A, Taniguchi S. J Am Ceram Soc 2002;85:1827.
[28] Dunand DC, Sommer JL, Mortensen A. Metall Trans A 1993;24: 2161.
[29] San Marchi C, Mortensen A. Metall Mater Trans A 1998;29:2819.
[30] Venkatesh TA, Dunand DC. Metall Mater Trans A 2000;31:781.
[31] Meyers MA, Chawla KK. Mechanical metallurgy. Englewood Cliffs (NJ): Prentice-Hall; 1984.
[32] Gibson LJ, Ashby MF. Cellular solids, structure and properties. 2nd ed. Cambridge, UK: Cambridge University Press; 1997.
[33] Bardella L, Genna F. Int J Solid Struct 2001;38:7235.
[34] Roberts AP, Garboczi EJ. Acta Mater 2001;49:189.
[35] Eshelby JD. Proc Roy Soc A 1957;241:376.
[36] Withers PJ, Stobbs WM, Pedersen OB. Acta Metall 1989;37:3061.
[37] Pettermann HE, Bohm HJ, Rammerstorfer FG. Composites B 1997;28:253.
[38] Ledbetter H, Kim S, Balzar D, Crudele S, Kriven W. J Am Ceram Soc 1998;81:1025.
[39] Herve E, Pellegrini O. Arch Mech 1995;47:223.
[40] Christensen RM, Lo KH. J Mech Phys Solids 1979;27:315.
[41] Kinra VK, Ker E. J Compos Mater 1982;16:117.
[42] Huang JS, Gibson LJ. J Mech Phys Solids 1993;41:55.